energy&fuels

Article

pubs.acs.org/EF

Pores in Marcellus Shale: A Neutron Scattering and FIB-SEM Study

Xin Gu,*,† David R. Cole,‡ Gernot Rother,§ David F. R. Mildner,∥ and Susan L. Brantley*,†,⊥

†Department of Geosciences, The Pennsylvania State University, University Park, Pennsylvania 16802, United States

‡School of Earth Sciences, The Ohio State University, Columbus, Ohio 43210, United States

§Chemical Sciences Division, Oak Ridge National Laboratory, Oak Ridge, Tennessee 37831, United States

∥NIST Center for Neutron Research, National Institute of Standards and Technology, Gaithersburg, Maryland 20899, United States

⊥Earth and Environmental Systems Institute, The Pennsylvania State University, University Park, Pennsylvania 16802, United States

ABSTRACT: The production of natural gas has become increasingly important in the United States because of the development of hydraulic fracturing techniques, which significantly increase the permeability and fracture network of black shales. The pore structure of shale is a controlling factor for hydrocarbon storage and gas migration. In this work, we investigated the porosity of the Union Springs (Shamokin) Member of the Marcellus Formation from a core drilled in Centre County, PA, USA, using ultrasmall-angle neutron scattering (USANS), small-angle neutron scattering (SANS), focused ion beam scanning electron microscopy (FIB-SEM), and nitrogen gas adsorption. The scattering of neutrons by Marcellus shale depends on the sample orientation: for thin sections cut in the plane of bedding, the scattering pattern is isotropic, while for thin sections cut perpendicular to the bedding, the scattering pattern is anisotropic. The FIB-SEM observations allow attribution of the anisotropic scattering patterns to elongated pores predominantly associated with clay. The apparent porosities calculated from scattering data from the bedding plane sections are lower than those calculated from sections cut perpendicular to the bedding. A preliminary method for estimating the total porosity from the measurements made on the two orientations is presented. This method is in good agreement with nitrogen adsorption for both porosity and specific surface area measurements. Neutron scattering combined with FIB-SEM reveals that the dominant nanosized pores in organic-poor, clay-rich shale samples are water-accessible sheetlike pores within clay aggregates. In contrast, bubblelike organophilic pores in kerogen dominate organic-rich samples. Developing a better understanding of the distribution of the water-accessible pores will promote more accurate models of water−mineral interactions during hydrofracturing.

1. INTRODUCTION

Growing energy needs and improved extraction capability around the world are motivating enhanced production of natural gas resources.[1,2] In 2011, natural gas was the fuel source for 24.8% of the electricity production and 30.0% of the primary energy production in the United States, and these proportions are expected to remain constant or increase over the next 25 years.[2] To meet the growing demand for energy, "unconventional" production techniques have been developed to access hydrocarbons in source rocks. The most successful new approach is the development of shale gas driven by the rapidly developing techniques of horizontal drilling and hydraulic fracturing. These techniques allow extraction of the natural gas that is present in the shales in fine pores.[3−5] A better understanding of the pore structures in gas shales could influence how both storage and transport of gas are managed and improve our ability to develop shale gas more effectively and safely.

Mesopores (2−50 nm) and micropores (<2 nm) are economically important to gas shale production because they constitute a large fraction of the shale porosity, and some of the pores may be filled with gas.[6,7] In addition, all of the pores provide surface sites for methane adsorption. The shape of the pores may also play an important role in gas/liquid transport, since round pores are much less likely to collapse from external pressure than cracklike or penny-shaped pores.[8,9] The structural integrity of pores also depends upon orientation.[10] Finally, the connectivity of pores is an essential factor to control gas transport pathways through shales.[11,12]

The Marcellus Shale is the most expansive shale gas play in the United States, covering six states in the northeastern region. It extends from upstate New York to Maryland and Virginia in the south and Ohio in the west, underlying 70% of Pennsylvania and much of West Virginia.[13] Few papers have reported the pore structure and distribution in this shale,[14,15] although other shales have been investigated.[4,11,16] The major difficulty in determining pore structures in low-porosity sedimentary and crystalline rocks is the small scale of the pores. For example, scanning electron microscopy (SEM) or transmission electron microscopy (TEM) photographs offer a resolution approaching 1 nm, but only small areas are scanned. Therefore, the areal coverage that is possible using this method is very small. Moreover, pore sizes and distributions from SEM images are difficult to quantify. In contrast, small-angle neutron scattering (SANS) and ultrasmall-angle neutron scattering (USANS) allow analysis of the pore structure averaged over centimeter-sized samples for pores from nanometers to micrometers in equivalent diameter.[17,18] Therefore, combining the electron microscopy and neutron scattering techniques leads to a more thorough assessment of the pore structures.

Received: May 14, 2014
Published: January 26, 2015

 © 2015 American Chemical Society

DOI: 10.1021/acs.energyfuels.5b00033
Energy Fuels 2015, 29, 1295−1308

Jin and co-workers reported the first observations of pore networks in Marcellus shale using neutron scattering.[19] They focused on samples from an outcrop of the shale in Huntingdon, PA, where they observed that the porosity increases significantly during shale weathering.[19] In the present work, we used the combination of SANS and USANS as well as focused ion beam SEM (FIB-SEM) to characterize the pore systems of Marcellus shale drilled at 300 m depth from central Pennsylvania. The drilled core allowed the investigation of samples with various organic content and mineralogy.

2. METHODS

Samples. In this study, we use the informal name Union Springs Member for the organic-carbon-rich basal unit of the Marcellus Formation (called the Shamokin Member in the literature).[20] This member is currently the most prominent drilling and production target for shale gas in Pennsylvania. Samples of the Union Springs Member were obtained from a core drilled in Bald Eagle State Park in Howard, PA, by the Appalachian Basin Black Shales Group at the Pennsylvania State University in conjunction with the Pennsylvania Topographic and Geologic Survey. The drill site (longitude −77.6562720, latitude 41.0317780) lies at the intersection of the Allegheny Plateau and the Valley and Ridge Province of the Appalachian Mountains, about 20 km east of the nearest shale gas wells (Figure 1). The Bald Eagle core is overmature with vitrinite reflectance (R_o) values of 2.2% (measured by the National Petrographic Service). Five samples were selected from the core: BE810, BE850, BE874, BE896, and BE910, where the numbers refer to the sampling depth below land surface in feet. Previous research identified the bulk chemistry of these samples.[19] This core was drilled to assess the extent and nature of Marcellus shale just outside of the major drilling areas in PA.

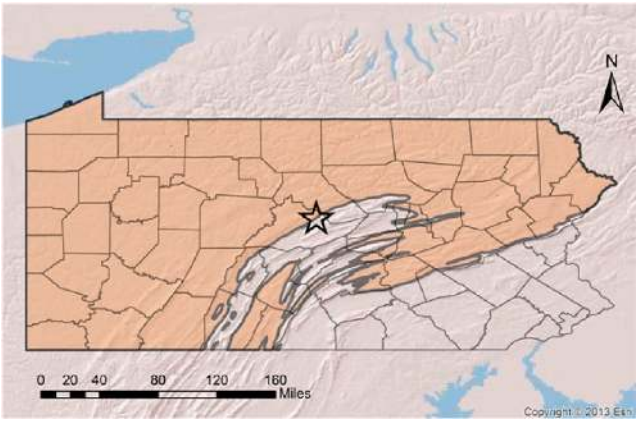

Figure 1. Map showing the location (tan color) of the Marcellus Formation in the subsurface of Pennsylvania (based on data from the Pennsylvania Department of Conservation and Natural Resources: http://www.dcnr.state.pa.us/topogeo/econresource/oilandgas/marcellus/marcellus_maps/index.htm). The Bald Eagle well (indicated by the star) was drilled in the Valley and Ridge Province by the Appalachian Basin Black Shales Group at the Pennsylvania State University.

Neutron Scattering. To prepare samples for scattering, the cores were cut parallel and perpendicular to the bedding. The samples were uniformly cut to be 250 μm thick on quartz slides as double-polished thick sections, as described previously.[21,22] The sections were sufficiently thin with high neutron transmission such that the multiple scattering was less than 10% for most samples.

SANS measurements were conducted on the NG7 spectrometer at the National Center for Neutron Research (NCNR) of the National Institute of Standards and Technology (NIST) (Gaithersburg, MD, USA). A neutron wavelength (λ) of 8.09 Å was used.[23] The scattering intensity (I) in units of cm^{-1} was measured at sample-to-detector distances of 1.0, 4.0, and 15.0 m. The momentum transfer is defined by $Q = 4\pi\lambda^{-1} \sin(\theta/2)$, where θ is the scattering angle and λ is the wavelength of the monochromatic neutron beam. Each thin section was mounted on a cadmium plate with a 1.27 cm aperture that defined the neutron beam incident on the sample.

USANS data were obtained on the perfect crystal BT5 USANS instrument at NCNR NIST.[24] The data were corrected for background,[22] and the normalized USANS data were desmeared and merged with the SANS data in absolute intensities according to the protocol of NIST.[25] The effect of multiple scattering was determined from the sample transmission (measured by BT-5) as discussed by Mang and Hjelm.[26] This multiscattering effect was eliminated using the MUX routine,[27] which is based on the theory developed by Schelten and Schmatz.[28] The range of measured Q values for SANS was 0.001 to 0.4 Å^{-1}, while the range for USANS was 3×10^{-5} to 0.003 Å^{-1}. For polydisperse porous media, Radlinski and co-workers found that the dimension of scatterers that contribute most to scattering at a given Q value is approximately $2.5/Q$.[29] Thus, for combinations of SANS and USANS (covering the range of Q from 3×10^{-5} to 0.4 Å^{-1}), the corresponding size range is 10 to 80 000 Å.

The intensity of scattered neutrons is proportional to the number of scatterers and the difference in scattering length density (SLD) between the phases. The SLD of phase j is given by

$$\rho_j^* = \frac{N_A d}{M_j} \sum_i s_i b_i \tag{1}$$

where $N_A = 6.022 \times 10^{23}$ mol^{-1} is Avogadro's number, d is the grain density (in g/cm^3), M_j is the molecular weight (in g/mol), s_i is the abundance of nucleus i in phase j, and b_i is the coherent scattering amplitude for nucleus i.[30] For a wide range of substances, the SANS data for geological materials and porous media can generally be interpreted using a two-phase approximation, where the two phases are the solid matrix and the pore space. Most minerals and rocks have SLDs on the order of $(3.5-4.5) \times 10^{-6}$ Å^{-2}, while the SLD of gas is close to 0. The SLD of the mineral matrix for the Marcellus shale samples was calculated from the elemental composition following procedures described in our previous study on Rose Hill shale[22] using the NIST SLD calculator (http://www.ncnr.nist.gov/resources/activation/). This calculation is based on the chemical composition and grain density of the bulk rock. The bulk chemical composition was calculated using the stoichiometry determined from the elemental chemistry of the bulk core samples (Table 1), and the grain density was calculated from the mineral composition (Table 2). It is notable that the SLD value of kerogen in the shale is similar to the SLD values of the mineral matrix (Table 1), so the organic and mineral phases may be treated as the same phase in the neutron scattering calculation.

Contrast-matching experiments were performed to assess water-accessible versus total porosity. Upon saturation of a rock sample with a mixture of H_2O and D_2O designed to have the same SLD as the rock matrix, the scattering due to matrix−pore contrast is lost,[22] and the scattering from water-accessible pores is eliminated (the D_2O:H_2O mass ratio used for each sample is shown in Table 1). Because the variations in SLD within minerals are small (Table 1), the observed difference between the scattering intensities of the dry and wet (soaked) samples is attributed to water-accessible porosity. To soak samples, they were equilibrated with contrast-matched fluid for 1 week in a quartz−sample−quartz "sandwich" as described previously.[22]

The intensity $I(Q)$ of SANS from many geological systems has been found to be inversely proportional to Q raised to an exponent n:

$$I(Q) = \frac{A}{Q^n} + B \tag{2}$$

where B is the Q-independent background. This power law relationship is well-known to be related to the fractal dimension of disordered systems.[31,32] A value of n between 2 and 3 represents a mass fractal with fractal dimensionality $D_m = n$, whereas a value of n between 3 and 4 characterizes a surface fractal with a fractal dimensionality D_s equal to $6 - n$.[3,30,33,34] A surface fractal is an

DOI: 10.1021/acs.energyfuels.5b00033
Energy Fuels 2015, 29, 1295−1308

Table 1. Calculated Scattering Length Densities

sample	relative elemental composition[a]	density (g/cm^3)	scattering length density (Å^{-2})	D_2O:H_2O mass ratio[b]
BE810	$Si_{107}Al_{36}Fe_9Ti_1Mg_4Ca_3K_9Na_2C_{22}H_{45}O_{314}S_4$	2.73	3.94×10^{-6}	69:31
BE850	$Si_{103}Al_{35}Fe_8Ti_1Mg_4Ca_{11}K_8Na_2C_{31}H_{45}O_{328}S_4$	2.73	4.00×10^{-6}	69:31
BE874	$Si_{111}Al_{33}Fe_8Ti_1Mg_4Ca_5K_8Na_3C_{21}H_{42}O_{322}S_3$	2.72	3.96×10^{-6}	69:31
BE896	$Si_{57}Al_{14}Fe_4Mg_2Ca_{93}K_3Na_1C_{101}H_{18}O_{415}S_2$	2.70	4.40×10^{-6}	73:27
BE910	$Si_{125}Al_{18}Fe_7Mg_4Ca_{11}K_4Na_1C_{76}H_{51}O_{336}S_5$	2.57	4.03×10^{-6}	69:31
kerogen	$C_{10}H_5O$	1.50	3.43×10^{-6}	–
quartz	SiO_2	2.65	4.19×10^{-6}	–
calcite	$CaCO_3$	2.71	4.69×10^{-6}	–
pyrite	FeS_2	5.01	3.81×10^{-6}	–
albite	$NaAlSi_3O_8$	2.62	3.97×10^{-6}	–
chlorite	$(Fe_{0.49}Mg_{0.14}Al_{0.31})_6(Si_{0.73}Al_{0.27})_4O_{10}(OH)_8$	2.65	3.21×10^{-6}	–
illite	$K_{0.72}(Al_{1.65}Fe_{0.28}Mg_{0.21})(Si_{3.23}Al_{0.77})O_{10}(OH)_2$	2.77	3.78×10^{-6}	–

[a]The elemental compositions were previously reported by Jin and co-workers.[19] [b]For contrast matching experiment.

Table 2. Mineral Content of the Marcellus Shale As Determined by X-ray Diffraction[a]

sample	quartz	plagioclase	carbonate	pyrite	illite	chlorite	amorphous + others	TOC
BE810	31.1	5.4	3	4.9	48.1	3	4.5	2.3
BE850	29.4	4.7	8.6	3.8	39.5	6.9	7.1	2.3
BE874	45.4	6.4	4.1	3.7	34.2	0.7	5.5	1.9
BE896	14.5	–	65.3	2.8	11.6	0.5	5.3	NM[b]
BE910	52	2.4	11.6	3.9	25.7	0.6	3.8	7.3

[a]X-ray diffraction (XRD) analysis was performed on powder samples (<150 μm) in a PANalytical Empyrean X-ray diffractometer at the Materials Characterization Laboratory, The Pennsylvania State University. The mineralogy was quantified by Rietveld analyses using the Jade software, and the concentration values reported here are mass percents normalized to 100%. Total organic carbon (TOC) contents were measured on a CHNS-O elemental analyzer (model EA 1110, Leco, St. Joseph, MI) at Penn State Agricultural Analytical Services Laboratory using ground samples (inorganic carbon was first removed using 2 N hydrochloric acid). The mineralogy data for BE810 and BE910 were previously published by Jin and co-workers.[19] [b]NM: not measured.

object of dimension L whose surface area varies as L^{D_s}, where D_s is a noninteger. A mass fractal is an object whose mass varies as L^{D_m}, where D_m is a noninteger.[30]

The dependence of the scattering intensity on the scattering angle is determined by the geometry of the pore–matrix interface at various length scales. This can be translated into a pore size distribution if the shape of individual pores is known or can be reasonably assumed. Under the assumption that the pores are spherical, a polydisperse spherical pore (PDSP) model has been applied to sedimentary rock.[30,35] However, we cannot obtain information about the pore shape and pore size distribution simultaneously by fitting the one-dimensional scattering data alone. Because of the lack of unique information about the pore size and shape from scattering, a combination of focused ion beam (FIB) milling and field-emission scanning electron microscopy (FE-SEM) was also used to obtain information about the size and shape of the pores, mineralogy, and the organic phase.

FIB-SEM. The core samples were cut using a low-speed saw and polished using sandpaper. Samples were mounted on SEM stubs using carbon paste. To achieve smooth faces for the cross-sectioned samples, a layer of platinum was deposited over the area to be milled using the FIB deposition system (FEI Quanta 200 eD Dual Beam FIB at Materials Characterization Laboratory, The Pennsylvania State University). During milling, the Ga^+ ion beam was maintained normal to the sample surface with the electron beam at an angle of 52° from the ion beam. The acceleration voltage for Ga^+ was 30 kV, and the beam current was 2.5 nA.

After the FIB milling, FE-SEM was performed on an FEI NanoSEM 630 FESEM microscope with an accelerating voltage in the range of 3–4 kV, and a landing energy in the range of 2–3.5 kV. The milled surface was maintained orthogonal to the detector. We used the backscattered electron (BSE) imaging mode with a vCD detector (low-voltage, high-contrast detector) to distinguish minerals, organic matter, and pores on the basis of differences in mean atomic number. The samples were also probed using energy-dispersive X-ray spectroscopy (EDS).

The biggest limitation of FIB-SEM is the observation scale. Because of cost and time constraints, only one or two trenches measuring 15 μm × 30 μm were cut for each sample, i.e., we analyzed only 8.85×10^{-5} of the area observed in our neutron scattering experiments (using a 1.27 cm diameter aperture). In view of the heterogeneities in the shale, the selected area viewed under FIB-SEM may not be representative.[4] However, SEM is the most advanced technique available that can image the pore system within shale.[36,37]

Nitrogen Adsorption. Nitrogen adsorption measurements were performed on a Micromeritics ASAP 2020 instrument (Micromeritics Instrument Corporation, Norcross, GA) at Materials Characterization Laboratory, The Pennsylvania State University, to analyze the surface area and porosity. The samples were degassed under vacuum at 105 °C for at least 8 h prior to measurement. The surface area was calculated according to Brunauer–Emmett–Teller (BET) theory,[38] and the pore volume distribution was calculated using density functional theory (DFT).[39] All of these calculations were completed using the Micromeritics software.

3. RESULTS

FE-SEM Observations on FIB Sections. The ion beam milling produced smooth and damage-free surfaces (Figures 2 and 3). XRD analysis demonstrated that Marcellus Formation shales largely contain quartz, illite, chlorite, and carbonates with minor but sometimes locally abundant pyrite (Table 2). In the BSE images, EDS analysis documented differences between the dark-gray areas, which apparently are kerogen (rich in carbon), the black areas, which are pores, and the light-gray areas, which are minerals. Qualitatively, the kerogen particles were observed to be more abundant in the organic-rich sample BE910 than in the other samples. Consistent with this, BE910 contained 7.3

DOI: 10.1021/acs.energyfuels.5b00033
Energy Fuels 2015, 29, 1295–1308

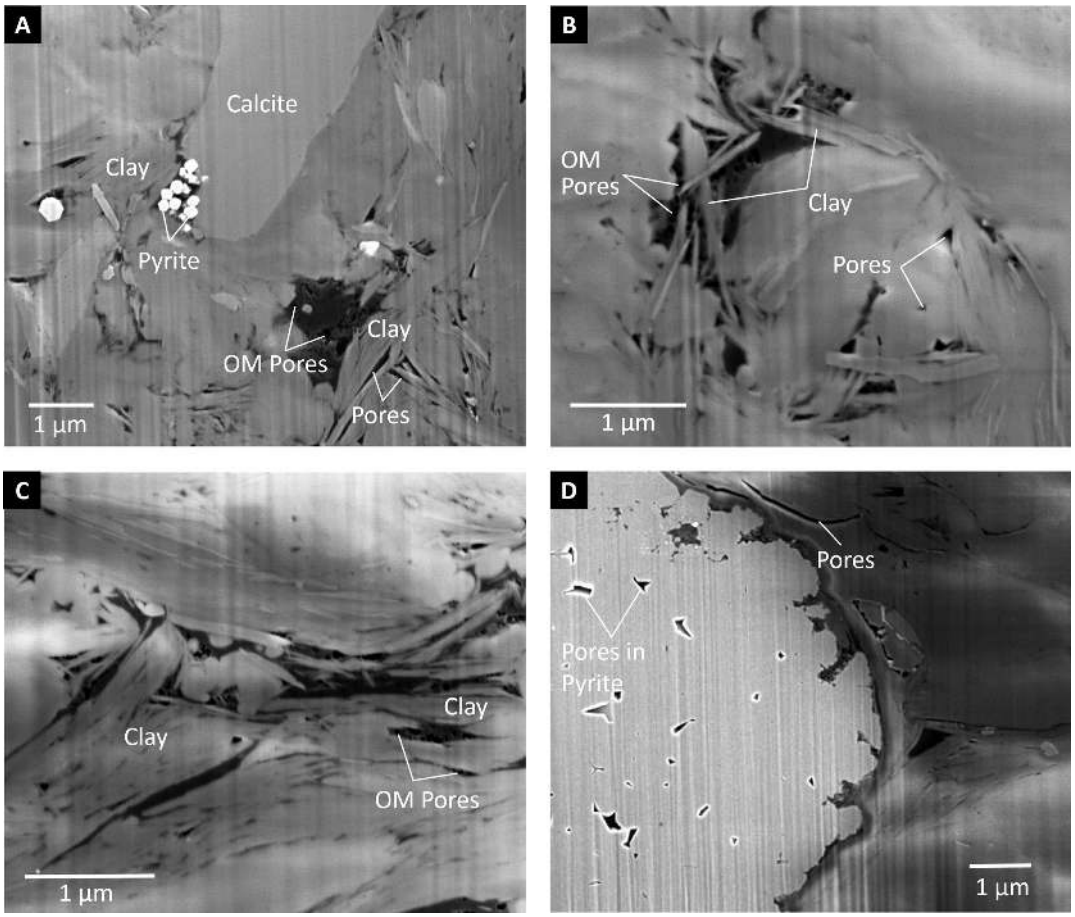

Figure 2. Backscattered electron (BSE) images of Marcellus shale sample BE850 cut (A, B) parallel and (C, D) perpendicular to the bedding plane. Samples were cross-sectioned using focused ion beam milling as described in text. In these images, black depicts pores, dark gray is kerogen, and light gray is the inorganic shale matrix containing clay, calcite, and quartz. Pyrite appears as the brightest particles. For the sample cut in the bedding plane (A, B), the clay particles are oriented randomly, while for the sample cut perpendicular to the bedding (C), the particles are roughly parallel to the bedding. Intraparticle pores in organic matter (A−D) or in pyrite (D) are generally equant, while pores between clay particles are slitlike. OM Pores are pores in organic matter (i.e., kerogen).

wt % total organic carbon (TOC) while the other samples contained 1.9−2.3 wt % (Table 2).

The organic matter observed in the Marcellus shale was mainly composed of amorphous kerogen, occurring as irregular patches or filling spaces between mineral grains (Figures 2 and 3). The sizes of kerogen particles were observed to vary from less than 1 μm to several microns. In contrast to the isolated kerogen aggregates observed in organic-poor samples (BE850), kerogen in the high-TOC sample (BE910) is homogeneously dispersed in the mineral matrix in the intergranular spaces (Figure 3A,B). For samples cut parallel to the bedding, the clay mineral platelets are randomly oriented (Figure 2A,B), while for samples cut perpendicular to the bedding, the clay mineral platelets are elongated parallel to the bedding (Figures 2C and 3D). Pyrite was observed to be present both as separated crystals (Figure 2D) and as fine-grained clusters of small octahedra in a framboid structure (Figure 3B).

Both pores in the mineral matrix and pores within the organic matter (OM) were observed in all of the Marcellus shale samples in this study. Framework pores aligned around rigid grains (quartz, calcite, or pyrite) with elongated shapes (Figures 2D and 3A,D), and triangular pores defined by clay mineral platelets (Figures 2A−C and 3C) are ubiquitous. Intragranular pores can be seen within pyrite crystals (Figure 2D). A few dissolution features were observed on carbonate grains (Figures 2A and 3D).

A large number of small, round OM pores on the order of a few nanometers to tens of nanometers in diameter were observed randomly dispersed within the kerogen of the organic-poor sample, making the OM look like a sponge (BE850, Figure 2). Interestingly, for the organic-rich sample (BE910, Figure 3A,B), the density of observable OM pores was lower in the kerogen grains. Consistent with this, Milliken and co-workers found that Marcellus shale samples with higher TOC have less detectable porosity within the OM.[15]

Anisotropy of the SANS Images. The scattering intensity was observed to be azimuthally asymmetric for sections cut perpendicular to the bedding but symmetric for parallel sections. For example, Figure 4 shows SANS data collected for section BE850 cut in the plane of the bedding, as well as one cut perpendicular to the bedding (Figure 4B). The plots are color-coded to show high (warm colors) or low (cool colors) scattered neutron count rates, as observed on the 2D detector at a distance of 4 m from the sample. In both plots, the intensity of neutrons decreases radially from the incident beam (at the center of the 2D pattern). However, the SANS pattern for the sample cut perpendicular to the bedding is anisotropic, indicating preferred orientation of scatterers, while that for the sample cut parallel to the bedding shows no preferred

DOI: 10.1021/acs.energyfuels.5b00033
Energy Fuels 2015, 29, 1295−1308

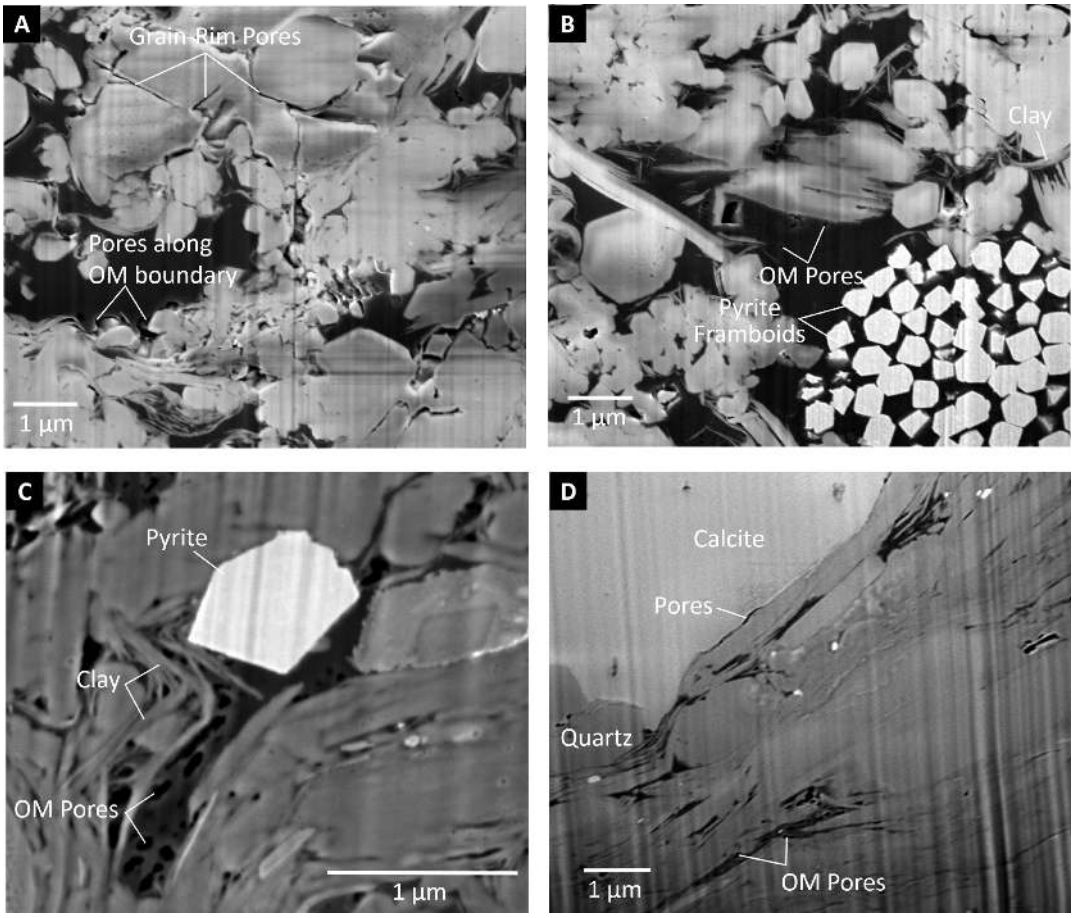

Figure 3. BSE images of (A, B) Marcellus shale samples relatively rich in organic matter (BE910) and (C, D) samples rich in carbonate (BE896). Samples were cross-sectioned using focused ion beam milling. The organic-rich shale sample (BE910) shows finely dispersed kerogen aggregates embedded in an inorganic matrix that contains pyrite (A, B). The carbonate-rich shale sample (BE896) shows limited porosity (D) in comparison with all of the other samples. OM Pores are pores in organic matter.

orientation. Radlinski and co-workers similarly found that the scattering from coal slices cut in the bedding plane was less intense than that from slices cut perpendicular to the bedding.[40]

To aid in quantifying the extent of the anisotropy, azimuthal scans ($0-2\pi$) of these 2D SANS patterns were taken in steps of 0.02π. Figure 5 shows the scattered intensity for sample BE850 at $Q = 0.02$ Å^{-1} as a function of the azimuthal angle ϕ. For the sample cut parallel to the bedding, the scattering intensity is essentially constant over the whole azimuthal ϕ range (Figure 5A), indicating random orientations of pores within the bedding plane. For the sample cut perpendicular to the bedding, the scattering intensity is concentrated at peaks at 0 and π (Figure 5B). The nonuniform intensity in the scattering pattern documents the preferential alignment of pores in the shale matrix.

Anisotropy can also be quantified with the Hermans orientation parameter (H), which provides a quantitative measure of the anisotropy and orientation of pores.[10] This parameter is defined as

$$H = \frac{3\langle\cos^2\phi\rangle - 1}{2} \tag{3}$$

where $\langle\cos^2\phi\rangle$ can be calculated from the integral

$$\langle\cos^2\phi\rangle = \frac{\int_0^{\pi/2} I(\phi)\cos^2\phi\sin\phi\,\mathrm{d}\phi}{\int_0^{\pi/2} I(\phi)\sin\phi\,\mathrm{d}\phi} \tag{4}$$

in which $I(\phi)$ is the scattering intensity as a function of the azimuthal angle ϕ (as shown in Figure 5). A pore system that has no preferred orientation (completely random) has $H = 0$, whereas $H = 1$ when the pores are perfectly aligned.

The H values (averaged) for the Marcellus samples cut parallel to the bedding are close to 0, ranging from 0.00 to 0.01. In contrast, the H values (averaged) for samples cut perpendicular to the bedding are significantly larger, ranging from 0.10 to 0.15 (Table 3). For the organic-poor samples, documented as blue symbols in Figure 6, the H values for total pores gradually decrease with pore dimension, indicating that many of the smaller pores—presumably dominated by pores within clay aggregates—are more oriented than larger pores (mainly framework pores around rigid grains). In contrast, for the organic-rich samples, documented as red symbols in Figure 6, the H values increase with pore dimension, suggesting that the small pores—presumably pores in organic matter—are more isotropic than the pores in clay aggregates.

Soaking the sample in a D_2O/H_2O mixture with the same SLD as the mineral matrix saturates water-accessible pores, leaving only water-inaccessible pores to be detected by scattering. As shown in Figure 6, the H values of the small

DOI: 10.1021/acs.energyfuels.5b00033
Energy Fuels 2015, 29, 1295−1308

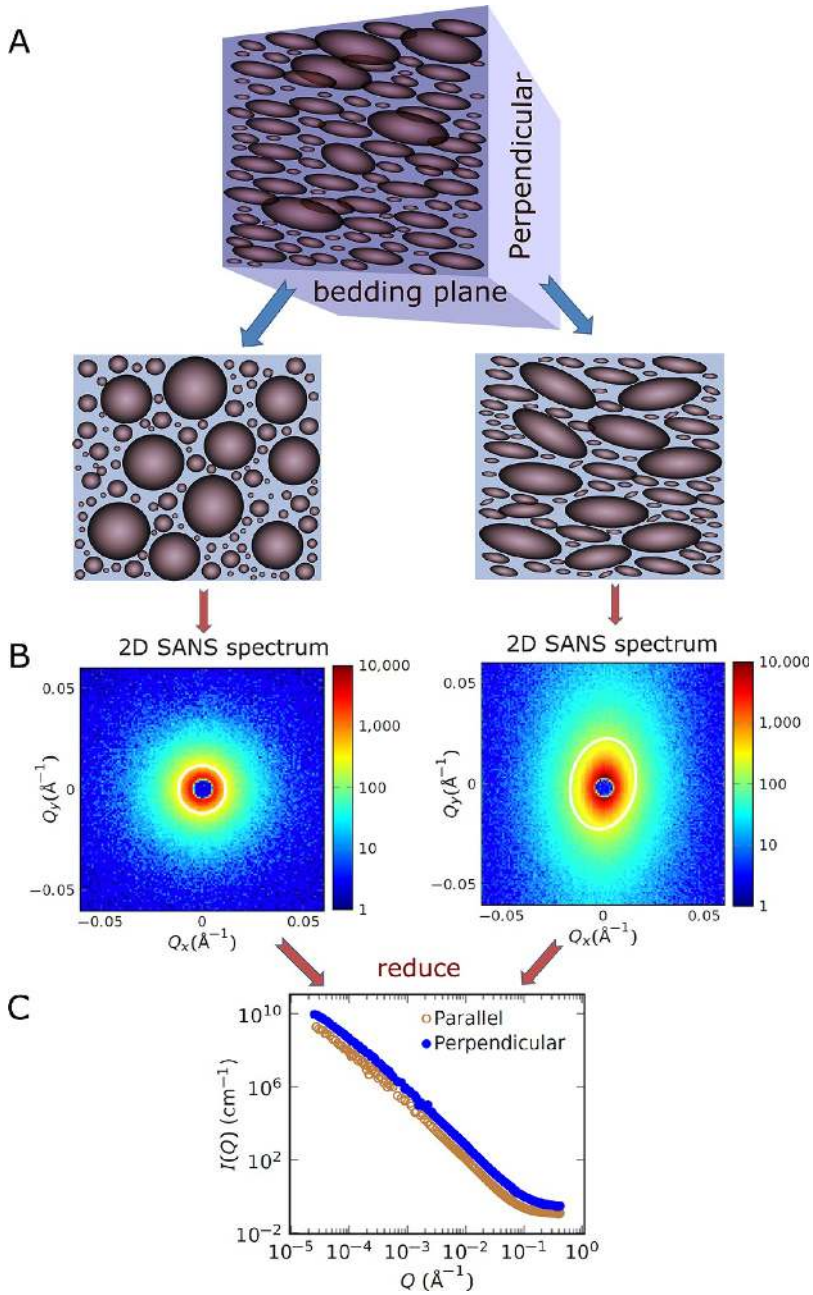

Figure 4. (A) Schematics showing the shapes of mineral grains in shale samples cut parallel or perpendicular to the bedding. (B) 2D SANS spectra for the BE850 sample cut parallel (left) and perpendicular (right): for the bedding-parallel sample, the scattering pattern is isotropic, and that for the bedding-perpendicular sample is anisotropic. The preferred direction in reciprocal space (the direction of the long axis of the elliptical contours shown in B) is orthogonal to the preferred direction in real space (the direction of grain alignment). (C) SANS and USANS neutron scattering intensities for sample BE850 cut parallel and perpendicular to the bedding, plotted as functions of the scattering vector Q. Error bars are too small relative to the data symbols to be apparent.

water-inaccessible pores (0.08 $Å^{-1}$ > Q > 0.01 $Å^{-1}$, corresponding to pore dimensions of 30 to 250 Å) in the organic-poor samples were 0.04 to 0.06 lower than the values for the total porosity. In contrast, the total and water-inaccessible pores in BE910, the sample with highest organic matter content, exhibited a much smaller discrepancy between the total and water-inaccessible porosities (0.02). This indicates that a large fraction of the small pores in BE910 are subspherical (almost isotropic with H values close to zero), and do not interconnect in the presence of water. On the basis of these characteristics, the majority of pores in BE910 are inferred to be hydrophobic, subspherical, and located in kerogen.

Quantification of the Pore System. On the basis of the PDSP model, the size distribution $f(r)$ and then the pore volume fraction φ within the bin defined by radii $[r_1, r_2]$ can be calculated as follows:

$$\varphi(r_1 \le r \le r_2) = \int_{r_1}^{r_2} Vf(r)\,\mathrm{d}r = \int_{r_1}^{r_2} \frac{4\pi r^3}{3} f(r)\,\mathrm{d}r \tag{5}$$

With these calculations, the surface area can also be calculated:

DOI: 10.1021/acs.energyfuels.5b00033
Energy Fuels 2015, 29, 1295−1308

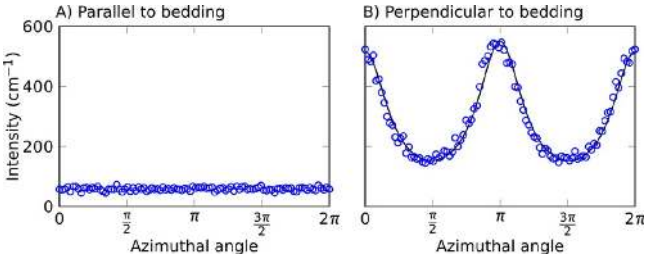

Figure 5. Plots of scattering intensity as a function of azimuthal angle (see the text). The 2D patterns in Figure 4B at $Q = 0.02$ Å^{-1} (sample-to-source distance = 4 m) for the BE850 sample cut (A) parallel and (B) perpendicular to the bedding (also see Figure 4) are plotted here. The sharp peaks at $\phi = 0$ and π for the sample cut perpendicular to the bedding indicate preferential orientation of the pores.

$$S(r_1 \leq r \leq r_2) = \int_{r_1}^{r_2} Sf(r)\,\mathrm{d}r = \int_{r_1}^{r_2} 4\pi r^2 f(r)\,\mathrm{d}r \tag{6}$$

Equations 5 and 6 are based on the implicit assumption that the pores are spherical. Neutron scattering is sensitive to entities in the scattering plane, and the resulting calculated porosities and surface areas are therefore projections onto that plane (entities include pores and surface bumps on the pore−grain interface). For samples cut parallel to the bedding, the scattering plane is the bedding plane: we refer to the porosity and specific surface area (SSA) calculated on the basis of eqs 5 and 6 as the "apparent porosity" and "apparent SSA" in the bedding plane, respectively. Here, $f(r)$ in eqs 5 and 6 is the ratio of the pore area to the total area in the 2D slice that is the scattering plane. Similarly, for samples cut perpendicular to the bedding, the pore information probed by neutron scattering is termed the apparent porosity and SSA for the plane normal to the bedding. Of course, for each section the sample has only one porosity; therefore, these inferred porosities are called "apparent".

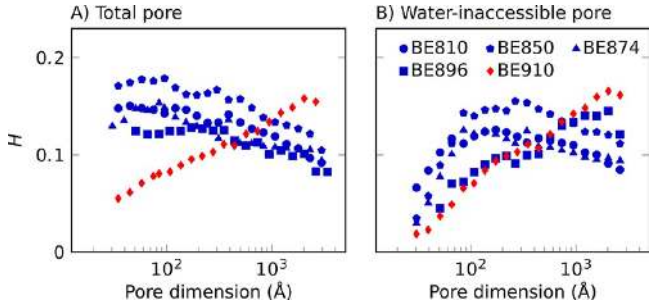

Figure 6. Hermans orientation parameters (H) for the perpendicular-cut samples plotted as functions of pore dimension for samples (A) before and (B) after soaking in a D_2O/H_2O mixture designed to match the average SLD of the rock. BE910 has a much higher TOC than the other samples.

The calculations of apparent porosity and SSA are summarized in Table 3. The apparent total porosity in bedding-perpendicular sections is significantly higher than the apparent total porosity in bedding-parallel sections. One way to conceptualize these results is to infer that the pores are largely present between bedding layers: the average apparent porosity varies from 20.1% for bedding-perpendicular sections to 4.3% for bedding-parallel sections (Table 3 and Figure 7). This result highlights that the true porosity can be misestimated from sections cut in certain orientations.

Table 3. Results from Neutron Scattering Analysis

sample	description[a]	T[b]	H[c]	n (whole)[d]	n (low Q)[e]	n (high Q)[f]	break (Å^{-1})[g]	porosity (%)[h]	SSA (m^2/g)[i]
BE810	parallel, dry	0.84	0.01	3.0	2.6	3.2	5.7×10^{-4}	4.8 ± 0.7	11.6 ± 3.7
	parallel, wet	0.85	0.01	2.9	2.6	3.0	6.2×10^{-4}	3.4 ± 0.7	3.7 ± 1.2
	perpendicular, dry	0.77	0.13	2.8	2.6	3.0	6.1×10^{-4}	24.3 ± 3.9	103.7 ± 21.7
	perpendicular, wet	0.78	0.11	2.9	2.7	3.0	5.9×10^{-4}	13.2 ± 2.1	35.7 ± 11.2
BE850	parallel, dry	0.93	0.01	3.0	2.6	3.1	5.4×10^{-4}	3.1 ± 0.5	8.0 ± 2.8
	parallel, wet	0.91	0.01	3.0	2.8	3.1	5.9×10^{-4}	2.0 ± 0.3	2.6 ± 0.6
	perpendicular, dry	0.71	0.15	2.9	2.7	3.1	6.2×10^{-4}	21.0 ± 3.6	86.7 ± 23.4
	perpendicular, wet	0.73	0.13	3.0	2.8	3.0	6.1×10^{-4}	10.7 ± 1.6	9.9 ± 3.3
BE874	parallel, dry	0.83	0.01	2.9	2.6	3.0	5.8×10^{-4}	4.0 ± 0.6	12.2 ± 3.9
	parallel, wet	0.89	0.01	3.0	2.8	3.0	5.8×10^{-4}	2.3 ± 0.3	2.4 ± 0.6
	perpendicular, dry	0.77	0.12	2.9	2.6	3.1	6.4×10^{-4}	19.1 ± 3.0	67.9 ± 18.7
	perpendicular, wet	0.80	0.10	3.0	2.6	3.0	5.9×10^{-4}	9.9 ± 1.5	13.2 ± 4.1
BE896	parallel, dry	1.00	0.00	3.0	2.6	3.1	6.3×10^{-4}	2.4 ± 0.4	3.6 ± 0.9
	parallel, wet	1.00	0.00	3.0	2.7	3.1	7.3×10^{-4}	1.4 ± 0.2	1.2 ± 0.3
	perpendicular, dry	0.82	0.11	2.9	2.6	3.1	5.5×10^{-4}	11.4 ± 1.7	18.9 ± 4.1
	perpendicular, wet	0.88	0.10	3.0	2.8	3.2	4.4×10^{-4}	3.9 ± 0.7	4.6 ± 1.4
BE910	parallel, dry	0.82	0.01	2.9	2.7	3.1	5.8×10^{-4}	7.2 ± 1.1	38.4 ± 8.7
	parallel, wet	0.88	0.01	2.9	2.9	3.1	5.0×10^{-4}	5.0 ± 1.1	24.8 ± 9.4
	perpendicular, dry	0.62	0.11	3.0	2.6	3.4	5.5×10^{-4}	24.5 ± 3.6	127.4 ± 27.9
	perpendicular, wet	0.66	0.10	3.0	2.7	3.3	5.3×10^{-4}	17.8 ± 2.7	86.7 ± 21.4

[a]Dry refers to measurements on samples before soaking in D_2O/H_2O. Data represent the total pores. Wet refers to measurements on samples after soaking in D_2O/H_2O. Data represent the water-inaccessible pores. Parallel and perpendicular refer to the orientation with respect to the bedding of the thin section. [b]T is the sample transmission; values of <0.9 indicate multiple scattering. [c]H is the Hermans orientation parameter; averaged values for three sample-to-detector distances are shown. [d]The exponent of Q in eq 2 (n) over the entire measurable range of Q (with an uncertainty of 0.1); $2 < n < 3$ indicates a mass fractal and $3 < n < 4$ a surface fractal. [e]The exponent n in the low-Q range (with an uncertainty of 0.1) [f]The exponent n in the high-Q range (with an uncertainty of 0.1) [g]Value of Q at the break in the slope (see the text) [h]Apparent porosity, as determined by the polydisperse spherical pore (PDSP) model. Uncertainties correspond to one standard error. [i]Apparent specific surface area (SSA), as determined by the PDSP model, assuming a shale density of 2.6 g/cm^3. Uncertainties correspond to one standard error.

DOI: 10.1021/acs.energyfuels.5b00033
Energy Fuels 2015, 29, 1295−1308

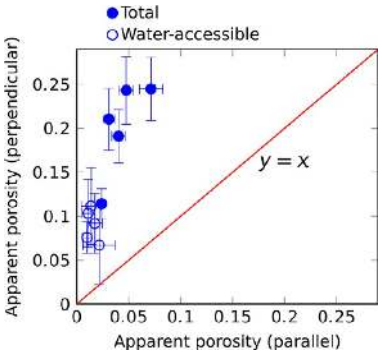

Figure 7. Apparent porosities (water-accessible or total as indicated) calculated from scattering from sections cut perpendicular to the bedding vs apparent porosities for sections cut parallel to the bedding for all five samples. Symbols lying closer to the $y = x$ line have equivalent porosities in the perpendicular- and parallel-cut sections. Statistical error bars indicate ±1 standard error as reported in Table 3.

We can also calculate the porosity and SSA for the whole sample using information gathered separately from bedding-perpendicular and bedding-parallel sections. For the sample cut parallel to the bedding plane, the incident beam lies along the normal to the bedding, and the measurement is sensitive to the pore size distribution in the bedding plane, so that the porosity φ_1 is determined within that plane. For the sample cut in a plane perpendicular to the bedding, the incident beam lies within the bedding plane, and the measurement is sensitive to the pore size distribution in the plane normal to the bedding, so that the porosity φ_2 is determined within that plane. There is no preferred direction within the bedding plane (Figures 4B and 5A), and we assume that the pore fraction varies smoothly with direction. Here we hypothesize that the total porosity of the sample can be estimated from the geometric average of the pore fractions in the three principal directions:

$$\varphi = (\varphi_1^2 \varphi_2)^{1/3} \tag{7}$$

Similarly, the specific surface area can be estimated as

$$\mathrm{SSA} = (\mathrm{SSA}_1^2 \cdot \mathrm{SSA}_2)^{1/3} \tag{8}$$

where SSA_1 and SSA_2 are the porosities of bedding-parallel and -perpendicular sections, respectively. This hypothesized method to calculate SSA from differently oriented sections was tested by a comparison with the BET surface area as discussed below.

Total pore size distributions obtained for shale samples are illustrated in Figure 8. Analysis of the combined SANS/USANS data provides quantitative pore size distributions in the pore size range from 10 Å to about 8 μm. In every case, the pore size distribution is very broad and includes contributions from every pore size within the entire range. The pore size distributions for the total pores (dry sample) and water-inaccessible pores (wet sample) are similar for the organic-rich BE910 sample; however, for the organic-poor samples, the volumes of water-inaccessible micropores (<2 nm according to IUPAC (1997) nomenclature) are much lower than those for total pores.

Quantitative analysis of the pore size distributions shows that for the organic-poor, clay-rich samples, the micropores constitute 12.5−14.5% of the total pores; furthermore, 81.6−93.2% of the micropores are water-accessible. In contrast, for the organic-rich sample, the micropores constitute 27.8% of the total pores, and only 35.1% of the micropores are water-accessible (Table 4). This fact implies that most of the scattering-detectable micropores in organic-rich shales consist of isotropic, organophyllic pores in kerogen. Also, micropores contribute most of the SSA (i.e., from 61.5% to 83.0%) in such shales (Table 4 and Figure 9). In contrast, for the carbonate-rich sample BE896, the proportion of micropores (2.1% for porosity and 19.0% for SSA) is significantly lower than for the other shale samples. Furthermore, the average pore dimensions determined by neutron scattering for all of the shale samples are in the nanometer range (2.9 to 9.8 nm), while the pore dimensions of the carbonate-rich sample (BE896) are higher (9.8 nm). For organic-poor, clay-rich samples, the pore dimensions of the water-accessible pores (2.6 to 2.7 nm) are smaller than those of the water-inaccessible pores (11.4 to 14.2 nm), which might be attributed to the small, hydrophilic pores in clay aggregates. In contrast, for the organic-rich samples, the pore dimensions of the water-accessible pores (2.5 nm) are similar to the average for the water-inaccessible pores (3.1 nm), indicating that the sample is dominated by small, organophyllic pores in kerogen.

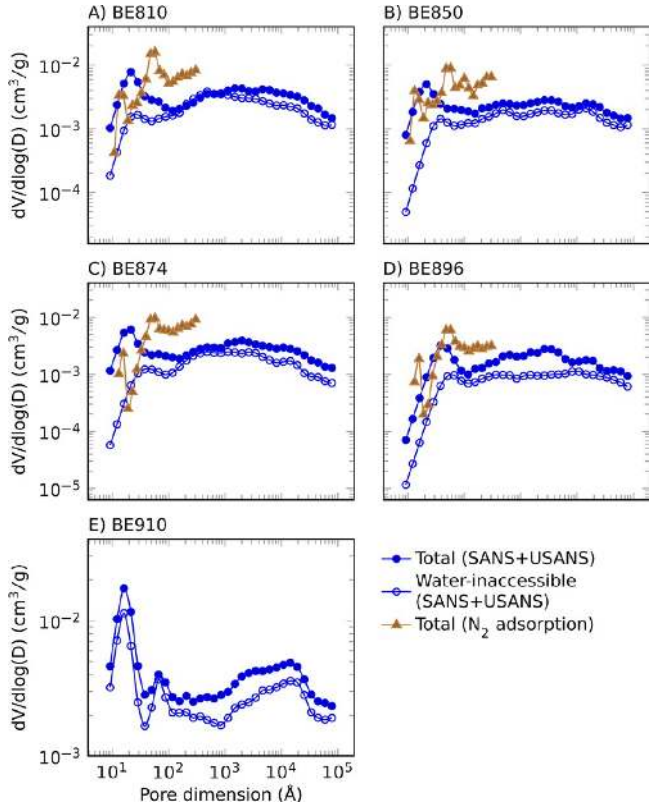

Figure 8. Pore size distributions as functions of pore dimension. The curves represent results obtained by fitting the PDSP model to the scattering data (blue) and from nitrogen adsorption data (brown).

The trends in the porosities inferred from N_2 adsorption show remarkable consistency with those in the total porosities calculated from the SANS/USANS data using eq 7 (Figure 10A). However, the pore size distributions derived from neutron scattering have more micropores and fewer mesopores compared with those derived from N_2 adsorption. Similar trends showing lower microporosity based on N_2 adsorption have been observed in other shales and attributed to the limited accessibility of micropores to N_2.[17,41] Some of this discrepancy may also be related to the sample preparation for N_2 sorption, which includes grinding of the sample (whereas scattering is

DOI: 10.1021/acs.energyfuels.5b00033
Energy Fuels 2015, 29, 1295−1308

Table 4. Porosities and Specific Surface Areas (SSAs) of the Marcellus Shale Samples

sample	pore type	porosity (%)[a]	SSA (m^2/g)[a]	micro porosity (%)[a,c]	micro SSA (m^2/g)[a,d]	average pore dimension (nm)[a,e]	porosity (%)[b]	SSA (m^2/g)[b]
BE810	total	8.0 ± 0.9	24.0 ± 6.4	1.0	14.8	5.1	6.8	15.7
	water- inaccessible	5.2 ± 0.8	7.0 ± 2.6	0.2	2.5	11.4		
	water- accessible	2.8 ± 1.2	17.0 ± 6.9	0.8	12.1	2.6		
BE850	total	5.8 ± 0.8	17.3 ± 5.9	0.7	10.7	5.2	5.2	11.0
	water- inaccessible	3.5 ± 0.4	3.9 ± 0.9	0.1	0.8	13.5		
	water- accessible	2.3 ± 0.9	13.3 ± 6.0	0.7	9.8	2.7		
BE874	total	6.7 ± 0.8	21.6 ± 6.2	1.0	14.6	4.8	5.7	10.2
	water- inaccessible	3.7 ± 0.4	4.0 ± 1.1	0.1	0.9	14.2		
	water- accessible	3.0 ± 0.9	17.6 ± 6.3	0.9	13.7	2.7		
BE896	total	4.0 ± 0.5	6.3 ± 1.4	0.1	1.2	9.8	2.9	6.6
	water- inaccessible	1.9 ± 0.2	1.8 ± 0.4	0.0	0.2	16.2		
	water- accessible	2.1 ± 0.5	4.5 ± 1.4	0.1	1.0	7.2		
BE910	total	10.6 ± 1.3	56.1 ± 12.0	2.9	46.6	2.9	NM[f]	NM[f]
	water- inaccessible	7.5 ± 1.2	37.0 ± 13.0	1.9	30.7	3.1		
	water- accessible	3.1 ± 1.8	19.1 ± 17.7	1.0	15.8	2.5		

[a]Derived from SANS/USANS data using the PDSP model. Uncertainties correspond to one standard error. [b]Derived from N_2 adsorption data. The porosity was calculated using DFT, and the surface area was calculated according to BET theory. [c]Porosity for pores <2 nm in size. [d]SSA for pores <2 nm in size. [e]The average pore dimension, defined as $4V/A$, where V is the pore volume and A is the surface area. [f]NM: not measured.

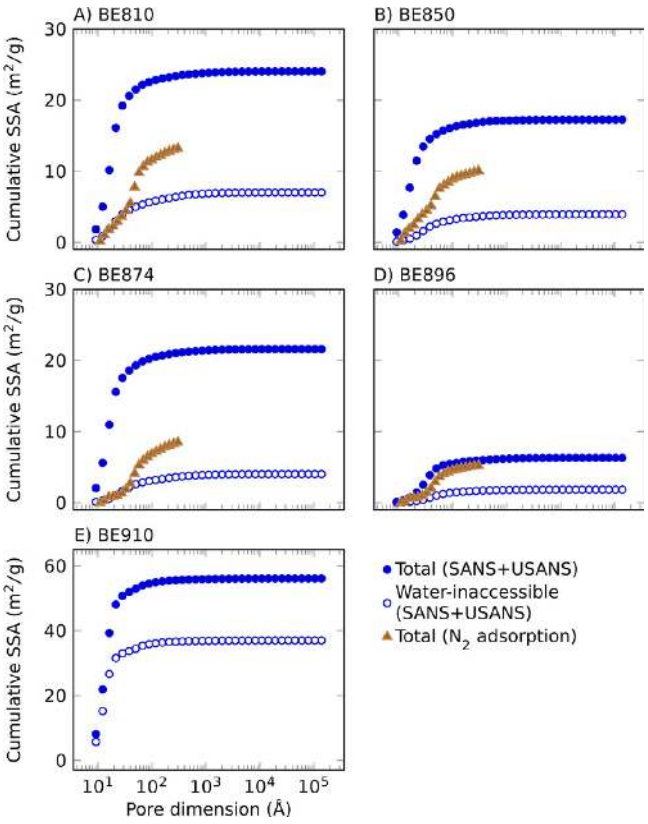

Figure 9. Cumulative SSAs calculated as functions of pore dimension for each of the five samples. The curves represent results obtained by fitting the PDSP model to the scattering data (blue) and from nitrogen adsorption data (brown). Organic-rich BE910 has a much higher total SSA and water-inaccessible SSA compared with the organic-poor samples.

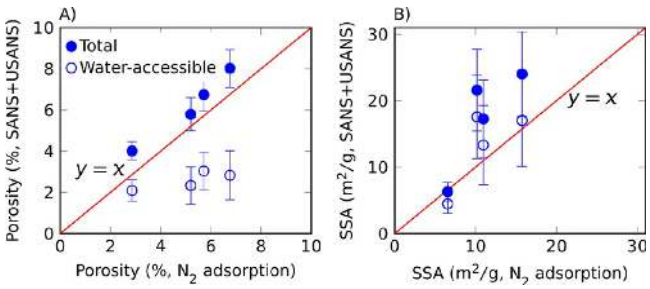

Figure 10. Comparison of (A) porosities and (B) specific surface areas obtained from combined SANS and USANS data as well as nitrogen adsorption. Generally, the porosities and SSAs probed by nitrogen adsorption are close to those measured by SANS and USANS. Statistical error bars indicate ±1 standard error as reported in Table 4

completed on a thin section sample).[42] Here the samples were ground to a particle size <150 μm. In contrast to the porosity, the total SSA values measured by SANS and USANS are larger than those measured by N_2 adsorption (Figure 10B), which again may largely be attributed to the limited accessibility of micropores to N_2. It is also worth noting that calculation of porosity and surface area from sorption or scattering data depends upon models that are based on an implicit assumption of a pore geometry and can incorporate assumptions about solid−fluid interactions. Therefore, differences in assumptions underlying the sorption and neutron scattering models are another likely contributor to the inconsistencies.

The Fractal Nature of Shale Porosity. The scattering curves show a power-law dependence in the small-Q range, i.e., a plot of log I versus log Q yields data aligned along a nearly straight line over 4 orders of magnitude in Q. The negative of the calculated slope of this line is the power exponent in eq 2 (Figure 4C). For $Q > 0.1$ Å^{-1}, a flat scattering background (B in eq 2) that is independent of Q was observed and can be attributed to incoherent scattering from hydrogen nuclei, small-scale nuclear density inhomogeneities, or both.[30] This scattering contribution was subtracted following standard procedures before further analysis.[30]

Regardless of whether the sample was cut parallel or perpendicular to the bedding plane, all of the samples yielded fractal dimensions approaching 3. These values indicate very rough interfaces between the pores and the mineral matrix (Table 3). Specifically, a scattering object with a fractal dimension of 3 can be considered either as a surface fractal with a surface that is so rough that the surface is space-filling or

DOI: 10.1021/acs.energyfuels.5b00033
Energy Fuels 2015, 29, 1295−1308

as a mass fractal comprising objects of a range of sizes such that it is infinitely polydisperse.[32]

A Kratky plot [i.e., a plot of $Q^2I(Q)$ vs Q] can be utilized to resolve the more subtle details of the scattering curve.[43] Figure 11 displays Kratky plots for two representative samples (BE850 and BE910) in wet and dry conditions. The wet samples show significantly lower scattering intensities than the dry samples over the whole range of Q. The profiles of the scattering curves are almost identical for scattering from the wet and dry samples of BE910, while for BE850, the scattering from the wet sample at high Q (above 0.08 $Å^{-1}$) is less intense than the scattering from the dry sample. Thus, most micropores are water-inaccessible in organic-rich BE910, but are water-accessible in organic-poor BE850.

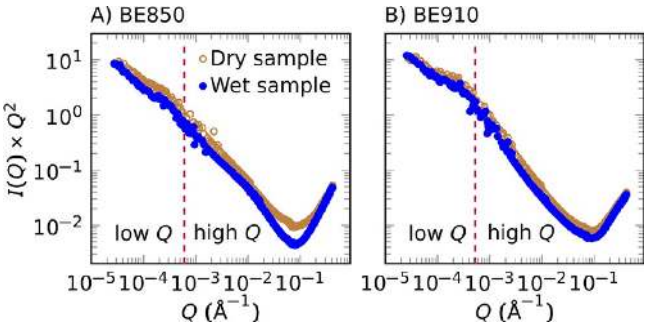

Figure 11. Kratky plots for (A) BE850 and (B) BE910 samples cut perpendicular to the bedding. In dry samples (before soaking in D_2O/H_2O), neutrons scatter from all of the pores (water-accessible and water-inaccessible), whereas in wet samples (after soaking in D_2O/H_2O), neutrons scatter only from water-inaccessible pores. Thus, the scattering intensity is lower for wet samples.

If the scattering followed the simple power law over the entire range in Q (as in eq 2), the Kratky plot would be a straight line (we are ignoring the background scattering at high Q, e.g., >0.1 $Å^{-1}$). However, a break in the slope occurs at $Q \approx 5 \times 10^{-4}$ $Å^{-1}$ (see the vertical dashed lines in Figure 11). The slopes in the low- and high-Q ranges as well as the break in the slope were calculated using piecewise regression. All of the samples show similar values of Q at the break in slope of [$(5.8 \pm 0.6) \times 10^{-4}$ $Å^{-1}$; Table 3]. This break is far from the overlap of the USANS and SANS data (0.001 $Å^{-1} < Q <$ 0.003 $Å^{-1}$) and thus is not due to poor statistics in the overlapping region or resolution effects. At Q values smaller than the break (see Figure 11), the exponent n (the negative of the slope) is smaller than 3, documenting a mass fractal. The mass fractal is attributed to the network of larger pores. At high Q, the dry samples comprise a surface fractal ($n > 3$). The surface fractal is attributed to bumps on pore−mineral interfaces.[44]

In either the low- or high-Q range, n for the wet sample is closer to 3 than that of the dry sample, indicating that the water-inaccessible pores are more polydisperse (or the surface is more space-filling) than the total pores. The organic-rich BE910 sample has a significantly higher n (i.e., a lower surface fractal dimension) at high Q compared with the more organic-poor samples. We infer this to be consistent with scattering from pores predominantly in kerogen for BE910. Thus, the surface of kerogen is less space-filling at the scale of mineral−water interfacial bumps compared with the surface of the mineral matrix.

4. DISCUSSION

Anisotropy of Marcellus Shale. In this study, SANS from the section cut perpendicular to the bedding shows a preferred orientation along the bedding plane over the whole measurable size range from a few angstroms to hundreds of nanometers. It is possible that this anisotropy extends to even larger scales, though we cannot assess it by USANS because these data are slit-smeared.

In contrast, scattering from sections cut parallel to the bedding are azimuthally symmetric. The isotropy of a scattering object can be explained if either (1) the shape of the pore−grain interfacial feature is isotropic, or (2) the shape is anisotropic but randomly oriented. Both cases may happen in the bedding plane of shale: the intraparticle pores in kerogen, pyrite, or the rare calcite are isotropic (Figures 2 and 3), while pores along grain boundaries are elongated but randomly oriented.

The features that cause asymmetric scattering in the perpendicular plane are likely present because of depositional processes for the shale: single particles, flocculates, and organomineralic aggregates ("marine snow") generally settle during mud accumulation to form parallel sheets of aggregates along the bedding during relatively low energy, stagnant flow, i.e., the flattened dimensions of the particles are parallel to the bedding, and the pores are slitlike. These pores are likely further flattened during burial.[37] Elongated grains are deposited with their long dimensions oriented approximately parallel to the bedding surface; indeed, the BSE images show that the clay minerals in Marcellus shale are aligned along the bedding plane (Figures 2C and 3D). However, the grains may have a random orientation within the bedding plane. Either way, the shale is likely to exhibit an isotropic distribution of scatterers within the bedding plane but an anisotropic distribution perpendicular to the bedding plane. The presence of symmetric scattering features in the samples cut parallel to the bedding but asymmetric features in the samples cut perpendicular to the bedding are consistent with previous observations on shaley rock[34] and outcrops of Marcellus shale.[19]

A negative correlation between the degree of anisotropy (H value) and pore dimension was observed for organic-poor samples (Figure 6). The anisotropy at the nanometer scale for the samples that are not organic-rich is most likely due to alignment of platelet-shaped clay minerals.[45] The lower detection limit of the pore dimension is about 5 nm for SEM, so the nanopores (<5 nm) within phyllosilicates are not observable. However, scanning transmission electron microscopy (STEM) images from studies on Haynesville shale clearly show that phyllosilicate pores are elongated along the bedding at the nanometer scale.[36] Larger pores include more isotropic pores along rigid grains (e.g., quartz, pyrite, and calcite), and more anisotropic pores along clay and kerogen (Figures 2 and 3). In contrast, for the organic-rich sample, many of the pores at the nanometer scale are isotropic and are likely subspherical pores in kerogen.

Pore Types in Marcellus Shale. In this study, a variety of techniques, including SANS/USANS, nitrogen gas adsorption, and FIB-SEM, were needed to fully characterize the pore structure of Marcellus shale. Each of these techniques can probe pores of a different size range: SANS/USANS (1 to 8000 nm, whole pore), nitrogen gas adsorption (nitrogen-gas-accessible pores in the size range of 2 to 300 nm), and FIB-SEM (5 to 2000 nm). Others have reported that porosities

DOI: 10.1021/acs.energyfuels.5b00033
Energy Fuels 2015, 29, 1295−1308

derived from SANS/USANS for shales have the same magnitude as those derived from N_2 gas adsorption (Figure 10A), but are significantly higher than those based on image analysis.[4,15]

Loucks and co-workers have categorized the pores within mudrock into three types on the basis of SEM observations: (1) pores within organic matter (OM pores), (2) pores within crystalline particles (intraP pores), and (3) pores between grains (interP pores).[4,37] We observed all of these in this study. Each type of pore may exhibit different neutron scattering features. As a first approximation, the sizes of the pores decrease in the order interP pores > OM pores ≈ intraP pores. Compaction is the most significant process in controlling the interP pore size and shape.[37] During compaction, interP pores around rigid grains (e.g., quartz, calcite, and pyrite) become elongated but remain relatively randomly distributed, while interP pores between soft and ductile grains (e.g., clay, kerogen) are elongated roughly parallel to the bedding. The shapes of intraP pores in mechanically strong minerals such as quartz are mainly controlled by their genesis and are less affected by compaction. For instance, intraP pores in pyrite framboids reflect the structure of the pyrite crystals within the framboid, while intraP pores in clays are sheetlike and roughly parallel to the bedding. Pores in kerogen are bubblelike or irregular in shape, generating symmetric scattering. Overall, the asymmetric scattering in perpendicular bedding results largely from the pores related to clay minerals (Figure 12).

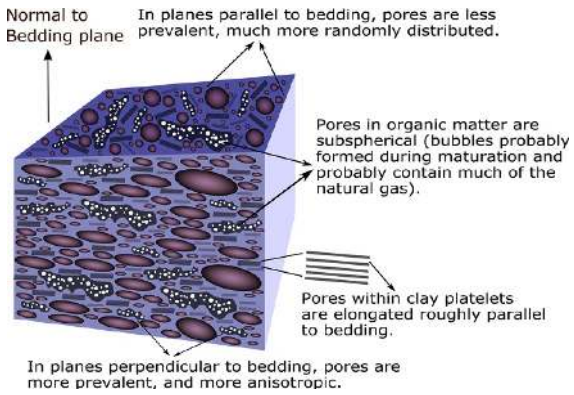

Figure 12. Schematic diagram of the pore structure in Marcellus shale.

SANS/USANS is a unique way to characterize the directionally dependent pore system in sedimentary rocks like shale. The apparent porosities measured in the sections cut perpendicular to the bedding are much higher than those measured in the plane of bedding. However, most studies on sedimentary rocks using scattering techniques have been completed on sections cut in one direction only, which may lead to an overestimation or underestimation of the porosity and SSA. For example, Clarkson and co-workers reported that the porosity for Marcellus shale (TOC = 1.57 wt %) cut parallel to the bedding was 3.55%, which is in the range of apparent porosity of the organic-poor, clay-rich samples cut parallel to the bedding in this study (Table 3, range from 3.1% to 4.8%).[46] Upon incorporation of the information from perpendicular-cut sections, the calculated values of total porosity for the same samples in our study range from 5.8% to 8.0%, indicating that the values reported by Clarkson and co-workers could be underestimated.[46]

The power-law relationship between Q and I demonstrates the random fractal nature of shale samples over several orders of magnitude in spatial dimension. A break in slope for the log I versus log Q plot is observed for all the samples. At low Q (larger pore dimension), the pore network is a mass fractal with D_m = 2.6 (on average), whereas at high Q (smaller pore dimension), the scattering object is a surface fractal with D_s close to 3. It has been argued that a break in slope may reflect two narrow distributions of polydisperse scatterers (pores), whereas no break in slope reflects a wider distribution, like a power-law distribution, of polydisperse scatterers.[47] Such breaks in slope have been observed in scattering curves of igneous and meta-igneous rocks[44,48] that have been analyzed by SANS/USANS as well as some shaley rocks.[33] However, Jin and co-workers found that there was no break in slope for Marcellus outcrop samples[19] and Rose Hill shale samples.[22] (It should be noted that the Marcellus samples studied by Jin and co-workers were from the Oatka Creek member of the Marcellus Formation,[19] whereas the samples in this study were from the Union Springs member.) Importantly, the outcrop samples studied by Jin and co-workers were derived from near the land surface, and thus were weathered and more porous than the samples studied here.[19] Jin and co-workers argued that some of the organic matter had been oxidized and removed in the Oatka Creek samples during near-surface weathering.[19] In that regard, both the Rose Hill[22] and Oatka Creek samples from Huntingdon[19] can be considered organic-poor shales. We infer that these differences in organic content result in different distributions of scatterers, which in turn affect the scattering profiles.

The pore distribution of the organic-rich BE910 sample is consistent with a large portion of the micropores occurring within the kerogen. However, SEM images show that the samples with high TOC in fact have less detectable porosity within the kerogen. As SEM can image only 5 nm pores, it is likely that much of the porosity in the kerogen is too small to image with SEM. Interestingly, Milliken and co-workers found a similar decreasing trend of SEM-detectable porosity with increasing TOC for Marcellus shale samples, while the porosity probed by N_2 adsorption increased with TOC.[15] Valenza and co-workers found that the SSA of the pores in kerogen could be as high as ~500 m^2/g of TOC in a mature shale,[49] again consistent with the existence of nanometer-sized pores in kerogen. Further studies based on TEM are being conducted to investigate nanometer-sized pores in kerogen directly.

Several studies based on SEM and TEM images have demonstrated that a large portion of the pores in kerogen in some shales are connected.[16,36] In contrast, our data indicate that pores in kerogen are not accessible to water in these Marcellus samples (Figure 8E and Table 4). This discrepancy could be explained if (1) the pores in kerogen are connected but the connections are not water-accessible because the entire pore is hydrophobic, and/or (2) the pores in kerogen grains are connected but the small flow pathway connections are hydrophobic, i.e., the pores in kerogen are connected at small scale but unconnected at large scale. It should be noted that the volume fraction of water-accessible pores in this study is between 30% and 52%, i.e., lower than the values reported for the Barnett shale.[50] This documents the variability in water accessibility among gas shale formations.

Implications. Shale contains a large portion of clay minerals, which are commonly oriented with basal planes along the bedding during sedimentation. Clays become

DOI: 10.1021/acs.energyfuels.5b00033
Energy Fuels 2015, 29, 1295−1308

increasingly aligned during compaction and diagenesis.[51] All of these processes typically result in anisotropic pore spaces, which are important contributors to elastic and seismic anisotropy.[52−54] These preferred orientations also affect the diffusivities of fluids in anisotropic rocks.[55,56] On the basis of the scattering observations reported here, much of this porosity is likely to be connected and hydrophilic unless the clay particles are heavily organic-coated. For example, as shown in Figure 10A, the water-accessible porosities are relatively similar for different samples of Marcellus shale from different depths, as if the inorganic matrices of samples (the hydrophilic porosities) do not vary significantly with depth. In contrast, the total porosities of the samples vary significantly with depth (Figure 10A). Thus, the water-inaccessible porosities must vary with depth. Since much of the porosity in the organic-rich BE910 sample can be attributed to subspherical pores in organic matter (Figure 6), we infer that the variations in water-inaccessible porosity with depth are largely due to variations in the subspherical pores in organic matter in the shale.

The subspherical nature of the pores in kerogen is consistent with the burial history of the rock. Specifically, the Marcellus Shale is thought to have been deposited in an epicontinental sea 389 million years ago. The organic carbon-rich mudstones of the Union Springs Member were deposited both as a hemipelagic basinal facies, and as the distal toe of a prograding delta clinoform.[57] As described by Engelder and Lash,[58] temperature and pressure increased during burial until the oil window was reached about 300 million years ago. By this time, most of the compaction had occurred, and the formation of slitlike pores was likely complete. After this period, the gas window was reached about 250 million years ago. The thermal decomposition of organic matter during maturation is a reasonable explanation for the observed intrakerogen porosity. This process is supported by many observations,[49,59] including experiments[60] and modeling.[61,62] This history is consistent with formation of pores in kerogen occurring after most of the compaction of the inorganic matrix, since the pores in kerogen are subspherical rather than flattened like the pores in the matrix (Figure 12).

Techniques such as horizontal drilling and hydraulic fracturing make the production of shale gas feasible in spite of the extremely low permeabilities, which are on the order of nanodarcies. The low water-accessible porosity, especially at larger pore size, observed in this study is consistent with these low permeabilities of shale. In the Marcellus Shale formation, hydrofracturing requires large amounts of water (4 to 5 million gallons of water per well) to open fractures in the shale.[63] After hydrofracturing, the flowback water is relatively dilute, but within weeks it generally becomes several orders of magnitude saltier than the original injectate.[64] Balashov et al.[64] have argued that brine is present as formation water, and that salt diffuses from small pores into the newly opened hydrofractures, explaining why the salt concentration increases during the first year of production of aqueous fluids. Such pores filled with brine are detectable by SANS/USANS, since the SLD of brine is close to that of gas and much smaller than that of the mineral matrix. Our observation, that the small pores associated with clay are water-accessible, is consistent with the interpretation that the brine is present initially at depth as capillary-bound water (i.e., immobilized in these very small pores), but nonetheless may be able to diffuse to fractures after hydrofracturing. A numerical diffusion model based on this conceptual model has successfully been used to explain the observed temporal changes in flowback chemistry for Marcellus shale-gas wells.[64] Thus, we infer that before hydrofracturing the water-accessible pores are partially filled by brine (±gas) while the water-inaccessible pores are filled with gas.

In addition, as proposed by Passey et al.,[65] there are two pore types in the shale: hydrophobic (largely in kerogen) and hydrophilic (largely in minerals or between minerals). In terms of natural gas, the pores within kerogen likely play the most important role in storage and permeability.[66] The existence of nanosized kerogen porosity, as suggested by this study, may mean that the transport of gas is not due to Darcy-type flow but rather due to diffusion and slip flow.[67] The larger SSA of these nanopores in kerogen will offer attractive sites for gas adsorption, which is critical in estimating the storage.[7]

Finally, we speculate that it is possible that the negative correlation we observed between kerogen pore width and TOC is consistent with high nucleation rates of gas bubbles relative to growth of the individual bubbles in the organic matter in the high-TOC shales. High nucleation rates would be expected in samples with the highest gas generation capacity and lowest connectivity of pores for removal of gas, both of which would be expected in a high-TOC shale. A better understanding of all these features could result in better techniques for hydraulic fracturing as well as better capabilities to estimate the gas storage and production rates. In addition, different hydrofracturing fluids might be developed to open hydrophilic interclay particle pores as opposed to hydrophobic intrakerogen pores or for use on high-TOC versus low-TOC shales.

■ AUTHOR INFORMATION

Corresponding Authors

*E-mail: xug102@psu.edu.

*E-mail: sxb7@psu.edu.

Notes

Disclaimer: The identification of commercial instruments in this paper does not imply recommendation or endorsement by the National Institute of Standards and Technology, nor does it imply that the equipment used is necessarily the best available for the purpose.

The authors declare no competing financial interest.

■ ACKNOWLEDGMENTS

We thank T. Clark and M. Yashinski at Material Characterization Laboratory at the Pennsylvania State University for FIB-SEM. We thank the Appalachian Basin Black Shales Group at the Pennsylvania State University and the Pennsylvania Topographic and Geologic Survey for providing shale samples. The SANS measurements at the National Institute of Standards and Technology were supported in part by the National Science Foundation under Agreement DMR-0944772. Research of X.G. and G.R. was sponsored by the Laboratory Directed Research and Development Program of Oak Ridge National Laboratory, managed by UT-Battelle, LLC, for the U.S. Department of Energy. S.L.B. acknowledges NSF Grant OCE 11-40159 for support for working on Marcellus shale, DOE OBES Grant DE-FG02-OSER15675 for work on porosity using neutron scattering, and Oak Ridge National Laboratory (acting under Contract DE-AC05-00OR22725 with the U.S. Department of Energy) for support for X.G. D.R.C. at OSU received support from the DOE Energy Frontier Research Center (EFRC) Nanoscale Control of Geologic CO2 through Grant 698077 (neutron scattering experiments) and NSF

DOI: 10.1021/acs.energyfuels.5b00033
Energy Fuels 2015, 29, 1295−1308

Dimensions: Division of Environmental Biology under grant DEB-1342701 (interpretation).

REFERENCES

(1) Holditch, S. A.; Perry, K.; Lee, J. *Unconventional Gas Reservoirs—Tight Gas, Coal Seams, and Shales*; Working Document of the National Petroleum Council on Global Oil and Gas Study; National Petroleum Council: Washington, DC, 2007

(2) *Annual Energy Outlook 2013*; U.S. Energy Information Administration: Washington, DC, 2013.

(3) Allen, A. J. Time-resolved phenomena in cements, clays and porous rocks. *J. Appl. Crystallogr.* **1991**, *24*, 624−634.

(4) Loucks, R. G.; Reed, R. M.; Ruppel, S. C.; Jarvie, D. M. Morphology, genesis, and distribution of nanometer-scale pores in siliceous mudstones of the Mississippian Barnett Shale. *J. Sediment. Res.* **2009**, *79*, 848−861.

(5) Strapoc, D.; Mastalerz, M.; Schimmelmann, A.; Drobniak, A.; Hasenmueller, N. R. Geochemical constraints on the origin and volume of gas in the New Albany Shale (Devonian-Mississippian), eastern Illinois Basin. *AAPG Bull.* **2010**, *94*, 1713−1740.

(6) Keller, L. M.; Holzer, L.; Wepf, R.; Gasser, P.; Munch, B.; Marschall, P. On the application of focused ion beam nanotomography in characterizing the 3D pore space geometry of Opalinus clay. *Phys. Chem. Earth, Parts A/B/C* **2011**, *36*, 1539−1544.

(7) Ambrose, R.; Hartman, R.; Diaz Campos, M.; Akkutlu, I.; Sondergeld, C. New pore-scale considerations for shale gas in place calculations. Presented at the SPE Unconventional Gas Conference, Pittsburgh, PA, USA, Feb 23−25, 2010.

(8) Bolton, A. J.; Maltman, A. J.; Fisher, Q. Anisotropic permeability and bimodal pore-size distributions of fine-grained marine sediments. *Mar. Pet. Geol.* **2000**, *17*, 657−672.

(9) Schaefer, C. E.; Towne, R. M.; Lazouskaya, V.; Bishop, M. E.; Dong, H. Diffusive flux and pore anisotropy in sedimentary rocks. *J. Contam. Hydrol.* **2012**, *131*, 1−8.

(10) Malwitz, M. M.; Lin-Gibson, S.; Hobbie, E. K.; Butler, P. D.; Schmidt, G. Orientation of platelets in multilayered nanocomposite polymer films. *J. Polym. Sci., Part B: Polym. Phys.* **2003**, *41*, 3237−3248.

(11) Slatt, R. M.; O'Brien, N. R. Pore types in the Barnett and Woodford gas shales: Contribution to understanding gas storage and migration pathways in fine-grained rocks. *AAPG Bull.* **2011**, *95*, 2017−2030.

(12) King, G. E. Hydraulic Fracturing 101: What Every Representative, Environmentalist, Regulator, Reporter, Investor, University Researcher, Neighbor and Engineer Should Know about Estimating Frac Risk and Improving Frac Performance in Unconventional Gas and Oil Wells. Presented at the SPE Hydraulic Fracturing Technology Conference, The Woodlands, TX, USA, Feb 6−8, 2012.

(13) USGS Marcellus Shale Assessment Team. *Information Relevant to the U.S. Geological Survey Assessment of the Middle Devonian Shale of the Appalachian Basin Province*; U.S. Geological Survey Open-File Report 2011-1298; U.S. Geological Survey: Reston, VA, 2011.

(14) Chalmers, G. R.; Bustin, R. M.; Power, I. M. Characterization of gas shale pore systems by porosimetry, pycnometry, surface area, and field emission scanning electron microscopy/transmission electron microscopy image analyses: Examples from the Barnett, Woodford, Haynesville, Marcellus, and Doig units. *AAPG Bull.* **2012**, *96*, 1099−1119.

(15) Milliken, K. L.; Rudnicki, M.; Awwiller, D. N.; Zhang, T. W. Organic matter-hosted pore system, Marcellus Formation (Devonian), Pennsylvania. *AAPG Bull.* **2013**, *97*, 177−200.

(16) Curtis, M. E.; Sondergeld, C. H.; Ambrose, R. J.; Rai, C. S. Microstructural investigation of gas shales in two and three dimensions using nanometer-scale resolution imaging. *AAPG Bull.* **2012**, *96*, 665−677.

(17) Clarkson, C. R.; Freeman, M.; He, L.; Agamalian, M.; Melnichenko, Y. B.; Mastalerz, M.; Bustin, R. M.; Radlinski, A. P.; Blach, T. P. Characterization of tight gas reservoir pore structure using USANS/SANS and gas adsorption analysis. *Fuel* **2012**, *95*, 371−385.

(18) Radlinski, A. P.; Ioannidis, M. A.; Hinde, A. L.; Hainbuchner, M.; Baron, M.; Rauch, H.; Kline, S. R. Angstrom-to-millimeter characterization of sedimentary rock microstructure. *J. Colloid Interface Sci.* **2004**, *274*, 607−612.

(19) Jin, L.; Mathur, R.; Rother, G.; Cole, D. R.; Bazilevskaya, E.; Williams, J.; Carone, A.; Brantley, S. L. Evolution of porosity and geochemistry in Marcellus Formation black shale during weathering. *Chem. Geol.* **2013**, *356*, 50−63.

(20) ver Straeten, C. A. Basinwide stratigraphic synthesis and sequence stratigraphy, Upper Pragian, Emsian and Eifelian stages (Lower to Middle Devonian), Appalachian Basin. In *Devonian Events and Correlations*; Becker, R. T., Kirchgasser, W. T., Eds.; Special Publications 278; The Geological Society of London: London, 2007; pp 39−81.

(21) Anovitz, L. M.; Lynn, G. W.; Cole, D. R.; Rother, G.; Allard, L. F.; Hamilton, W. A.; Porcar, L.; Kim, M. H. A new approach to quantification of metamorphism using ultra-small and small angle neutron scattering. *Geochim. Cosmochim. Acta* **2009**, *73*, 7303−7324.

(22) Jin, L.; Rother, G.; Cole, D. R.; Mildner, D. F. R.; Duffy, C. J.; Brantley, S. L. Characterization of deep weathering and nanoporosity development in shale—A neutron study. *Am. Mineral.* **2011**, *96*, 498−512.

(23) Glinka, C. J.; Barker, J. G.; Hammouda, B.; Krueger, S.; Moyer, J. J.; Orts, W. J. The 30 m small-angle neutron scattering instruments at the National Institute of Standards and Technology. *J. Appl. Crystallogr.* **1998**, *31*, 430−445.

(24) Barker, J. G.; Glinka, C. J.; Moyer, J. J.; Kim, M. H.; Drews, A. R.; Agamalian, M. Design and performance of a thermal-neutron double-crystal diffractometer for USANS at NIST. *J. Appl. Crystallogr.* **2005**, *38*, 1004−1011.

(25) Kline, S. R. Reduction and analysis of SANS and USANS data using Igor Pro. *J. Appl. Crystallogr.* **2006**, *39*, 895−900.

(26) Mang, J. T.; Hjelm, R. P. Fractal networks of inter-granular voids in pressed TATB. *Propellants, Explos., Pyrotech.* **2013**, *38*, 831−840.

(27) Monkenbusch, M. DEMUX/MUX—Removal of multiple-scattering from small-angle data. *J. Appl. Crystallogr.* **1991**, *24*, 955−958.

(28) Schelten, J.; Schmatz, W. Multiple-scattering treatment for small-angle scattering problems. *J. Appl. Crystallogr.* **1980**, *13*, 385−390.

(29) Radlinski, A. P.; Boreham, C. J.; Lindner, P.; Randl, O.; Wignall, G. D.; Hinde, A.; Hope, J. M. Small angle neutron scattering signature of oil generation in artificially and naturally matured hydrocarbon source rocks. *Org. Geochem.* **2000**, *31*, 1−14.

(30) Radlinski, A. P. Small-angle neutron scattering and the microstructure of rocks. *Rev. Mineral. Geochem.* **2006**, *63*, 363−397.

(31) Wong, P.-z.; Bray, A. J. Porod scattering from fractal surfaces. *Phys. Rev. Lett.* **1988**, *60*, 1344.

(32) Schmidt, P. W. Small-angle scattering studies of disordered, porous and fractal systems. *J. Appl. Crystallogr.* **1991**, *24*, 414−435.

(33) Mildner, D. F. R.; Hall, P. L. Small-angle scattering from porous solids with fractal geometry. *J. Phys. D: Appl. Phys.* **1986**, *19*, 1535−1545.

(34) Mildner, D. F. R.; Rezvani, R.; Hall, P. L.; Borst, R. L. Small-angle scattering of shaly rocks with fractal pore interfaces. *Appl. Phys. Lett.* **1986**, *48*, 1314−1316.

(35) Hinde, A. L. PRINSAS—A Windows-based computer program for the processing and interpretation of small-angle scattering data tailored to the analysis of sedimentary rocks. *J. Appl. Crystallogr.* **2004**, *37*, 1020−1024.

(36) Curtis, M. E.; Ambrose, R. J.; Sondergeld, C. H.; Rai, C. S. Transmission and scanning electron microscopy investigation of pore connectivity of gas shales on the nanoscale. Presented at the North American Unconventional Gas Conference and Exhibition, The Woodlands, TX, USA, June 14−16, 2011.

(37) Loucks, R. G.; Reed, R. M.; Ruppel, S. C.; Hammes, U. Spectrum of pore types and networks in mudrocks and a descriptive

DOI: 10.1021/acs.energyfuels.5b00033
Energy Fuels 2015, 29, 1295−1308

classification for matrix-related mudrock pores. *AAPG Bull.* **2012**, *96*, 1071−1098.
(38) Brunauer, S.; Emmett, P. H.; Teller, E. Adsorption of gases in multimolecular layers. *J. Am. Chem. Soc.* **1938**, *60*, 309−319.
(39) Olivier, J. P. Improving the models used for calculating the size distribution of micropore volume of activated carbons from adsorption data. *Carbon* **1998**, *36*, 1469−1472.
(40) Radlinski, A. P.; Mastalerz, M.; Hinde, A. L.; Hainbuchner, A.; Rauch, H.; Baron, M.; Lin, J. S.; Fan, L.; Thiyagarajan, P. Application of SAXS and SANS in evaluation of porosity, pore size distribution and surface area of coal. *Int. J. Coal Geol.* **2004**, *59*, 245−271.
(41) Mastalerz, M.; He, L. L.; Melnichenko, Y. B.; Rupp, J. A. Porosity of coal and shale: insights from gas adsorption and SANS/USANS techniques. *Energy Fuels* **2012**, *26*, 5109−5120.
(42) Brantley, S. L.; Mellott, N. P. Surface area and porosity of primary silicate minerals. *Am. Mineral.* **2000**, *85*, 1767−1783.
(43) Anovitz, L. M.; Cole, D. R.; Rother, G.; Allard, L. F.; Jackson, A. J.; Littrell, K. C. Diagenetic changes in macro- to nano-scale porosity in the St. Peter Sandstone: An (ultra) small angle neutron scattering and backscattered electron imaging analysis. *Geochim. Cosmochim. Acta* **2013**, *102*, 280−305.
(44) Navarre-Sitchler, A. K.; Cole, D. R.; Rother, G.; Jin, L.; Buss, H. L.; Brantley, S. L. Porosity and surface area evolution during weathering of two igneous rocks. *Geochim. Cosmochim. Acta* **2013**, *109*, 400−413.
(45) Voltolini, M.; Wenk, H. R.; Mondol, N. H.; Bjorlykke, K.; Jahren, J. Anisotropy of experimentally compressed kaolinite−illite−quartz mixtures. *Geophysics* **2009**, *74*, D13−D23.
(46) Clarkson, C. R.; Solano, N.; Bustin, R. M.; Bustin, A. M. M.; Chalmers, G. R. L.; He, L.; Melnichenko, Y. B.; Radlinski, A. P.; Blach, T. P. Pore structure characterization of North American shale gas reservoirs using USANS/SANS, gas adsorption, and mercury intrusion. *Fuel* **2013**, *103*, 606−616.
(47) Martin, J. E.; Hurd, A. J. Scattering from fractals. *J. Appl. Crystallogr.* **1987**, *20*, 61−78.
(48) Buss, H. L.; Brantley, S. L.; Scatena, F. N.; Bazilievskaya, E. A.; Blum, A.; Schulz, M.; Jimenez, R.; White, A. F.; Rother, G.; Cole, D. Probing the deep critical zone beneath the Luquillo Experimental Forest, Puerto Rico. *Earth Surf. Processes Landforms* **2013**, *38*, 1170−1186.
(49) Valenza, J. J.; Drenzek, N.; Marques, F.; Pagels, M.; Mastalerz, M. Geochemical controls on shale microstructure. *Geology* **2013**, *41*, 611−614.
(50) Ruppert, L. F.; Sakurovs, R.; Blach, T. P.; He, L.; Melnichenko, Y. B.; Mildner, D. F. R.; Alcantar-Lopez, L. A USANS/SANS study of the accessibility of pores in the Barnett Shale to methane and water. *Energy Fuels* **2013**, *27*, 772−779.
(51) Day-Stirrat, R. J.; Aplin, A. C.; Srodon, J.; Van der Pluijm, B. A. Diagenetic reorientation of phyllosilicate minerals in Paleogene mudstones of the Podhale Basin, southern Poland. *Clays Clay Miner.* **2008**, *56*, 100−111.
(52) Sayers, C. M. The elastic-anisotropy of shales. *J. Geophys. Res.: Solid Earth* **1994**, *99*, 767−774.
(53) Johansen, T. A.; Ruud, B. O.; Jakobsen, M. Effect of grain scale alignment on seismic anisotropy and reflectivity of shales. *Geophys. Prospect.* **2004**, *52*, 133−149.
(54) Almqvist, B. S. G.; Mainprice, D.; Madonna, C.; Burlini, L.; Hirt, A. M. Application of differential effective medium, magnetic pore fabric analysis, and X-ray microtomography to calculate elastic properties of porous and anisotropic rock aggregates. *J. Geophys. Res.: Solid Earth* **2011**, *116*, No. B01204.
(55) Van Loon, L. R.; Soler, J. M.; Muller, W.; Bradbury, M. H. Anisotropic diffusion in layered argillaceous rocks: A case study with opalinus clay. *Environ. Sci. Technol.* **2004**, *38*, 5721−5728.
(56) Nakashima, Y.; Kamiya, S.; Nakano, T. Diffusion ellipsoids of anisotropic porous rocks calculated by X-ray computed tomography-based random walk simulations. *Water Resour. Res.* **2008**, *44*, No. W12435.
(57) Kohl, D.; Slingerland, R.; Arthur, M.; Bracht, R.; Engelder, T. Sequence stratigraphy and depositional environments of the Shamokin (Union Springs) Member, Marcellus Formation, and associated strata in the Middle Appalachian Basin. *AAPG Bull.* **2014**, *98*, 483−513.
(58) Engelder, T.; Lash, G. G. Marcellus Shale Play's vast resource potential creating stir in Appalachia. *Am. Oil Gas Rep.* **2008**, *52*, 76−87.
(59) Mastalerz, M.; Schimmelmann, A.; Drobniak, A.; Chen, Y. Y. Porosity of Devonian and Mississippian New Albany Shale across a maturation gradient: Insights from organic petrology, gas adsorption, and mercuty intrusion. *AAPG Bull.* **2013**, *97*, 1621−1643.
(60) Chen, J.; Xiao, X. M. Evolution of nanoporosity in organic-rich shales during thermal maturation. *Fuel* **2014**, *129*, 173−181.
(61) Jarvie, D. M.; Hill, R. J.; Ruble, T. E.; Pollastro, R. M. Unconventional shale-gas systems: The Mississippian Barnett Shale of north-central Texas as one model for thermogenic shale-gas assessment. *AAPG Bull.* **2007**, *91*, 475−49.
(62) Modica, C. J.; Lapierre, S. G. Estimation of kerogen porosity in source rocks as a function of thermal transformation: Example from the Mowry Shale in the Powder River Basin of Wyoming. *AAPG Bull.* **2012**, *96*, 87−108.
(63) Brantley, S. L.; Yoxtheimer, D.; Arjmand, S.; Grieve, P.; Vidic, R.; Pollak, J.; Llewellyn, G. T.; Abad, J.; Simon, C. Water resource impacts during unconventional shale gas development: The Pennsylvania experience. *Int. J. Coal Geol.* **2014**, *126*, 140−156.
(64) Balashov, V. N.; Engelder, T.; Xin, G.; Fantle, M. S.; Brantley, S. L. A Model Describing Flowback Chemistry Changes with Time after Marcellus Shale Hydraulic Fracturing. *AAPG Bull.* **2015**, *99*, 143−154.
(65) Passey, Q. R.; Bohacs, K. M.; Esch, W. L.; Klimentidis R.; Sinha S. From oil-prone source rock to gas-producing shale reservoir—Geologic and petrophysical characterization of unconventional shale-gas reservoirs. Presented at the CPS/SPE International Oil and Gas Conference, Beijing, China, June 8−10, 2010; SPE 131350.
(66) Wang, F. P.; Reed, R. M. Pore networks and fluid flow in gas shales. Presented at the SPE Annual Technical Conference and Exhibition, New Orleans, LA, USA, Oct 4−7, 2009.
(67) Javadpour, F.; Fisher, D.; Unsworth, M. Nanoscale gas flow in shale gas sediments. *J. Can. Pet. Technol.* **2007**, *46*, 55−61.

DOI: 10.1021/acs.energyfuels.5b00033
Energy Fuels 2015, 29, 1295−1308